View Online / Journal Homepage / Table of Contents for this issue
Nanoscale
Dynamic Article Links

Cite this: *Nanoscale*, 2012, **4**, 600

www.rsc.org/nanoscale

PAPER

Conductive scanning probe microscopy of nanostructured Bi_2Te_3

Tewfik Souier,[a] Guang Li,[a] Sergio Santos,[a] Marco Stefancich[ab] and Matteo Chiesa*[ab]

Received 21st September 2011, Accepted 7th November 2011
DOI: 10.1039/c1nr11366f

Downloaded by Massachusetts Institute of Technology on 15 June 2012
Published on 06 December 2011 on http://pubs.rsc.org | doi:10.1039/C1NR11366F

In order to explain the unique thermoelectric properties of bulk nanocomposite p-type bismuth antimony telluride, its structural and electrical properties are investigated using transmission electron microscopy (TEM) and atomic force microscopy with a conductive probe (C-AFM). The material is observed to contain both nano- and micro-sized grains with sizes varying from 10 nm to 3 μm. This unique structure promotes phonon scattering, thereby decreasing the thermal conductivity to below 1 W mK^{-1} at room temperature. Moreover, the C-AFM data show that the electrical conductivity of nanosized grains is higher than the bulk value and reaches 1600 S cm^{-1}. This results in a moderate increment of the overall electrical conductivity, thereby increasing the figure of merit (ZT) up to 1.4 at 100 °C. In addition to demonstrating a powerful scanning probe microscopy (SPM) based investigation technique that requires minimal sample preparation, our findings contribute towards better understanding of the enhancement of thermoelectric properties of nanocomposite thermoelectric materials.

I. Introduction

Thermoelectric (TE) energy conversion is a very attractive method for environmentally cooling and recovering energy from waste heat. Solid-state TE devices have potential applications in air conditioning, refrigeration, combustion engines, and more recently in the conversion of sunlight into electricity.[1] Indeed, a promising flat-panel solar thermal to electric power conversion based on the thermoelectric effect and optical concentrators was proposed as an alternative to photovoltaic technology. For these applications, it is required to attain a high thermoelectric efficiency. This efficiency depends on the dimensionless figure-of-merit,[2] ZT, as well as electrical and thermal contact resistances between the TE element and the host electrodes.[3–5]

The dimensionless ZT of a thermoelectric element is given by $ZT = S^2\sigma T/\kappa$. S is the Seebeck coefficient, σ the electrical conductivity, T the temperature and κ the thermal conductivity. One traditional way to increase ZT consists of minimizing the lattice thermal conductivity κ_L while maximizing the material's electrical conductivity and thermopower. Nanoscale effects have been established so far as the means for enhancing ZT in thermoelectrics as reported both in experimental and theoretical studies.[6–13] These studies provide a proof of principle, but limitations in applicability of this technology persist, partly due to the difficulties with scalability and cost.

For near room temperature applications, up to 200 °C, bismuth telluride based single crystal solid solutions, including p-type BiSbTe and n-type BiTeSe, with ZT ≈ 1, still remain the best materials used for thermoelectric systems. Although the resulting crystalline materials present good thermoelectric properties, they have poor mechanical properties. Recently,[14,15] p-type nanostructured $Bi_xSb_{2-x}Te_3$, with a peak of ZT of 1.4, was obtained by ball milling and hot pressing the alloyed crystalline ingots. Poudel[16] has achieved a similar ZT by ball milling elemental chunks of Bi, Sb, and Te into alloy nanopowders first and then hot pressing them into dense bulk nanostructures. These achievements are an important step towards cost-reduction of high ZT TE materials. The ZT enhancement is believed to be related to the unique microstructure of the nanograined bulk material. In this paper we present a study of the microstructure of the $(Bi,Sb)_2Te_3$ nanograined composite by means of scanning and transmission electron microscopes, SEM and TEM. We present also new characterisation techniques, with nanometre-resolution, of both structural and electrical properties of thermoelectric materials based on atomic force microscopy, AFM. These qualitative results will guide and improve the materials processing of nanocomposite TE materials and lead to further increases in ZT.

II. Material and methods

1. Material preparation

Nanopowders were made by ball milling bulk p-type BiSbTe alloy ingots. Bulk disk samples (1.25 cm to 2.5 cm in diameter and 2 mm to 3 mm in thickness) were made by hot pressing the nanopowders loaded into graphite dies. The samples were

[a]*Laboratory of Energy and Nanosciences, Masdar Institute of Science and Technology, Abu Dhabi, UAE*
[b]*Department of Mechanical Engineering, Massachusetts Institute of Technology, 77 Massachusetts Avenue Cambridge, MA, 02139-4307, USA. E-mail: mchiesa@mit.edu*

This journal is © The Royal Society of Chemistry 2012

Published on 06 December 2011 on http://pubs.rsc.org | doi:10.1039/C1NR11366F
Downloaded by Massachusetts Institute of Technology on 15 June 2012

polished for structural characterization, electrical and thermal conductivity measurements. After hot pressing, both sides of the disk were grinded using sand paper and mechanically polished (MP) using 5 wt% 0.05 μm alumina suspensions. This initial surface was employed as a reference for the polishing process (S1). Following the MP step, a chemical mechanical polishing (CMP) was performed (S2) in order to reveal the microstructure. The slurry used here is 5 wt% 0.05 μm colloid silica. The pH was adjusted to 5 by nitric acid additions. We tried to add 1% of hydrogen peroxide (H_2O_2) and 0.1% benzotriazol (BTA) for passivation and corrosion inhibition. It was reported that this surface condition increases the wettability and subsequently metallization that enhances the contact between the TE materials and electrode.[24] Moreover, the CMP operation offers a smooth surface, erases the scratches and reveals the grain boundaries.[17] Fig. 1 shows the microstructure of the Bi_2Te_3 nanocomposite after hot pressing (Fig. 1a and b) and after polishing (Fig. 1c). The images were obtained using a high resolution Quanta FEG (SEM) under high vacuum and at 10 kV. It seems that the material consists mainly of grains with size ranging between 1 μm and 3 μm. In some areas, submicron or nano-grains, with a size of 100 nm or less, are observed (Fig. 1b). The EDX analysis in several micro-sized and nano-sized grains illustrates that the nanocomposite is a ternary alloy of bismuth antimony telluride, BiSbTe (Fig. 1d). The typical weight chemical composition is Bi: 0.26, Te: 0.48 and Sb: 0.26.

2. Experimental methods

2.1. Transmission electron microscopy. TEM lamellas are obtained from nanostructured Bi_2Te_3 by means of Focused Ion Beam, FIB. A copper grid holds the lamella in our Titan 80-300 transmission electron microscope from FEI Company. All the TEM images are recorded under 300 kV using STEM mode (Z-contrast imaging) and Fischione high angle annular dark field.

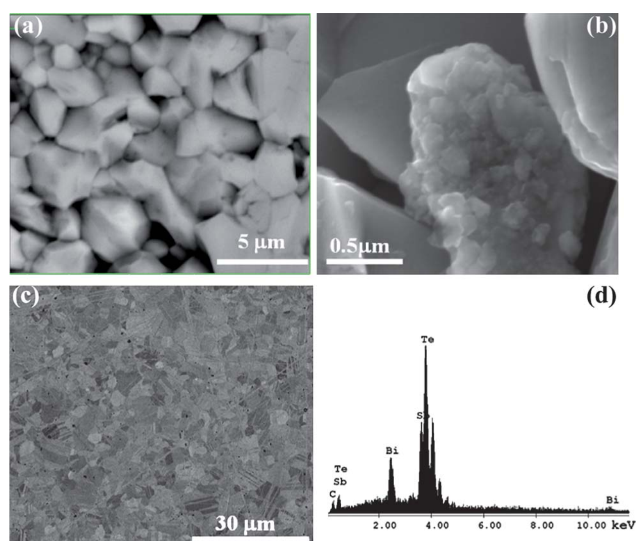

Fig. 1 SEM images of the nanocomposite Bi_2Te_3 sample obtained at 10 keV voltage, and using a backscattered detector. (a and b) show micro-sized and nano-sized grains obtained after hot-pressing and before polishing, (c) shows the microstructure of the surface after mechanical and chemical–mechanical polishing CMP steps. The typical EDS profile is presented in (d) showing the chemical composition of the nanocomposite sample after CMP polishing.

2.2. Atomic force microscopy. The setup employed in our investigation is an AFM MFP-3D from Asylum Research mounted on "stand-alone configuration". The scanner is capable of a maximum horizontal scanning of 90 μm in closed loop and a vertical scanning range up to 15 μm.

The ORCA holder is used for both AFM topography and electrical CS-AFM imaging. All of the images are obtained in contact mode.

The AFM-topography images are obtained in open circuit (the tip and the sample are electrically connected). We recorded simultaneously the height, the deflection (normal movements of the cantilever) and the friction (lateral movements of the cantilever) images.

For CS-AFM imaging, the tip and the sample are electrically connected. A current sensing (CS) module (ORCA) is added to the microscope for simultaneous topography (height) and current measurements in contact mode. The amplifier of the CS module in the AFM head was fully customized for measurements with a dual-gain (1 GΩ and 1 MΩ), allowing current sensing in the range of 1 pA up to 10 μA.

The topography images are carried out using a silicon tip, CD-NCHR from Nanosensor®, covered with doped diamond. The resonant frequency of the tip is about 350 kHz and the spring constant is estimated at 30 N m^{-1} by thermal tuning. The diamond coating consists of p-type boron doping with an electrical resistivity of 0.003–0.005 Ω cm. The coating is approximately 100 nm in thickness and the tip radius is estimated at 150 nm by SEM imaging (Fig. 2a).

CS-AFM imaging is performed in contact mode under ambient air conditions by using two tips: a CD-NCHR diamond coated tip from Nanosensor® (see the above description) and an

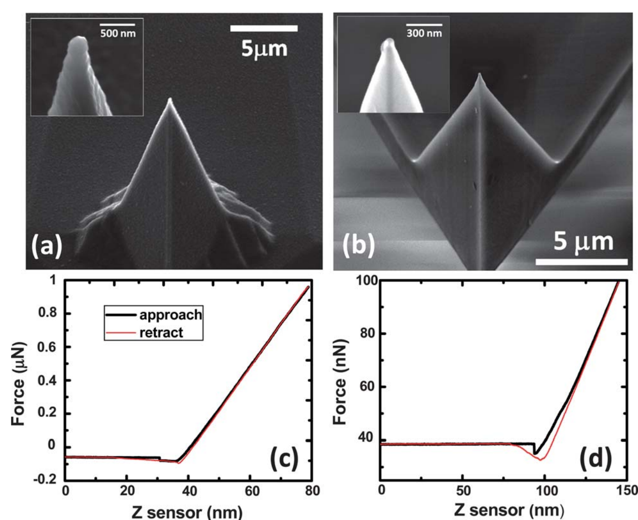

Fig. 2 SEM images of the two conductive coated AFM tips used for both AFM and C-AFM imaging, with a diamond tip (a) and an iridium tip (b). Force–distance curves using a diamond tip (c) and an iridium tip (d). The force curves are used to understand the tip–sample mechanical interaction and quantify the area of mechanical and electrical contact.

Published on 06 December 2011 on http://pubs.rsc.org | doi:10.1039/C1NR11366F
Downloaded by Massachusetts Institute of Technology on 15 June 2012

ASYLEC iridium coated silicon tip from Asylum Research. The resonant frequency of the iridium tip is about 75 kHz, with a spring constant of 3 N m^{-1} and a tip radius of 30 nm (Fig. 2b). The diamond coated tip is found to be more mechanically stable and wear resistant and is used for scanning large areas up to 80 × 80 μm. The iridium tip is used for scanning small areas, typically 1 × 1 μm.

2.3. Model for estimation of the local electrical conductivity

2.3.1. Model assumptions. In order to extract the electrical conductivity from the CS-AFM data, we employ a model that describes the electrical transport within the nano-contact tip–sample. The main assumptions for our model are presented below with a short explanation.

(1) The electrical contact between the tip and the sample is Ohmic.

Two situations are observed while imaging metallic surfaces with CS-AFM. Highly conducting areas are attributed to a tiny metallic junction between the tip apex and the sample (ohmic contact), whereas the insulating regions correspond to tunnelling junctions.[18,19] The tunnelling regime results from the existence of an insulating barrier between the tip apex and the sample, most likely a native oxide layer or other contaminations. Houze[18] demonstrated that the tunnelling model leads to a realistic parameter (barrier height and width) only for resistance values higher than 1 MΩ.

In the present study, the estimated values of the resistance, extracted from CS-AFM data, are on the order of kΩ which is a range consistent with the hypothesis of an ohmic tip–sample contact rather than the existence of a tunnelling junction. The explanation for this is that our CS-AFM experiments were carried out immediately after the specimen preparation and most likely before the formation of a thick native oxide layer. This is confirmed by the obtained *I–V* curves recorded on as-polished specimens showing an ohmic behaviour, whereas after a few weeks of aging in air, the *I–V* curves are non-linear, suggesting the formation of an oxide layer acting as a tunnelling barrier (Fig. 3).

(2) The nano-contact tip–sample is mechanically and electrically stable.

It is important to note that the CS-AFM technique is usually used for qualitative analysis. Very few quantitative studies are reported.[20–23] The main reason for this is due to the lack of reproducible results due to the convolution between the sample roughness and the tip apex, as well as mechanical instability. We demonstrated in parallel studies that if the tip radius is greater than 25–30 nm, the measurements are reproducible and can provide quantitative data without issues involving mechanical tip instability.[24–26]

Concerning the electrical contact stability, the CS-AFM imaging was performed in contact mode under relatively high forces in order to record a reproducible and stable current. Indeed, it has been reported that large forces are required to measure a stable and reproducible current by CS-AFM on gold substrate.[27]

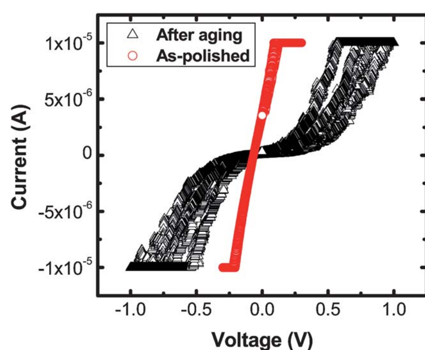

Fig. 3 *I–V* spectra obtained by using diamond conductive AFM tip on thermoelectric sample after polishing (red dots) and after 3 weeks aging in contact with air (black triangles). The two *I-V* spectra are obtained in the same sample with the same experimental conditions.

2.3.2. Description of the model. The electrical resistance extracted from current maps (dividing the current by the applied voltage) is the equivalent resistance of the tip, the sample and the contact resistance. Since the contact area is in the nanoscale range, the extracted electrical resistance can be approximated to the nano-contact resistance between the tip and the sample R_{nc}. Thus, the electrical conductivity can be estimated using either the Maxwell formula[28] or Sharvin's law[29] depending on the size of the nano-contact. If the electron mean free path l_e is lower than the contact radius a, the nanocontact resistance is given by Maxwell's formula:

$$R_M = \frac{\rho}{2a} \quad (1)$$

while, $l_e < a$, the Sharvin resistance is:

$$R_S = \frac{4\rho l_e}{3\pi a^2} \quad (2)$$

In this study, since the typical contact radius ranges from 4 nm to 14 nm (see below), the Sharvin and Maxwell contact resistances are in the same order of magnitude, *i.e.*, both the ballistic and the diffusive aspect of electronic transport are relevant. According to the work of Wexler[30] and Nikolic,[31] the nano-contact resistance can be written as:

$$R_{nc} = R_S + \frac{1 + 0.83 \times l_e/a}{1 + 1.33 \times l_e/a} R_M \quad (3)$$

where ρ is the electrical resistivity, a is the radius of the tip–sample contact and l_e is the elastic or inelastic electron mean free path reported to be 60 nm.[32] Using our model, the estimated value of the electrical conductivity depends on the true value of the electron mean free path of our sample. This is clearly a limitation of the model. Nevertheless we are mainly interested in deriving the order of magnitude of the electrical conductivity and comparing it with the values obtained at the macroscopic scale.

2.3.3. Estimation of the tip–sample contact radius. In order to model the mechanical interaction between the tip and the sample, force curves in different areas have been recorded using AFM probes. Fig. 2c and d show typical approach-retraction curves obtained with diamond and iridium probes respectively. The adhesion forces extracted from the force curves are 35 nN (diamond) and 7 nN (iridium). For the C-AFM imaging, we used large contact forces in order to avoid mechanical instabilities of the tip–sample interaction: 100 nN (for diamond) and 10–20 nN

 This journal is © The Royal Society of Chemistry 2012

Published on 06 December 2011 on http://pubs.rsc.org | doi:10.1039/C1NR11366F
Downloaded by Massachusetts Institute of Technology on 15 June 2012

(for iridium). The values of the force are chosen in order to achieve a reproducible and stable current without inducing plastic deformation of the tip or the sample.

The mechanical radius of the tip–sample contact is evaluated using Derjaguin, Muller, and Toporov—DMT[33] approximation:

$$a_{\mathrm{DMT}} = \left(\frac{3r_{\mathrm{tip}}(P + 2\pi w r_{\mathrm{tip}})}{4E^*}\right)^{1/3} \quad (4)$$

where P is the tip–substrate contact force, r_{tip} is the tip radius (150 nm for diamond and 30 nm for iridium tips), w is the work adhesion (adhesion force extracted from force curves, Fig. 2c and d), and E^* is the effective elastic modulus given by:

$$E^* = \left(\frac{1 - \upsilon_{\mathrm{s}}^2}{E_{\mathrm{s}}} + \frac{1 - \upsilon_{\mathrm{tip}}^2}{E_{\mathrm{tip}}}\right)^{-1} \quad (5)$$

where $\upsilon_{\mathrm{tip}} = \upsilon_{\mathrm{s}} = 0.33$ is the Poisson's ratio of the tip and the sample, $E_{\mathrm{s}} = 40$ GPa is the Young modulus of the sample (value obtained by nano-indentation, results not shown) and E_{tip} is the Young modulus of the tip (1200 GPa: diamond and 528 GPa: iridium). Using these values, the contact radius is estimated to be approximately 3–4 nm for the iridium tip and 12 nm for the diamond tip.

The DMT approximation is valid in the elastic regime of both the tip and the sample. The yield strength was estimated to be in the range of 500 to 800 MPa by nanoindentation (results not presented). By using the estimated DMT radius, the applied pressure during CS-AFM imaging lies between 200 and 300 MPa. Moreover in a previous study, we have demonstrated that once the AFM tip is mechanically stable, it can handle a higher pressure than its yield strength.[24] For these reasons, the tip and sample behave elastically and the DMT approximation is plausible.

If plastic deformation occurs, the contact diameter in the plastic regime can be estimated using the following expression:

$$a_{\mathrm{plastic}} = \left(\frac{4P}{\pi H}\right)^{1/2} \quad (6)$$

where H is the hardness of the softer material (Bi_2Te_3) and is about 1 GPa (value obtained by nanoindentation experiments). Under these conditions, the expected values of the contact radius are 6 nm for the iridium tip and 14 nm for the diamond tip. These two values may be used to evaluate the error made on the estimated electrical conductivity if the sample is deformed plastically.

III. Experimental results and discussion

3.1. Structural characterisation with TEM

Fig. 4 shows typical STEM images obtained using a Fischione high angle annular dark detector (HAADF) at different magnifications. Besides the micro-sized grains detected using SEM, grains with submicron size (few 100 nm) have been observed as shown in Fig. 4a and b. These grains are polygonal and have the same composition as the bulk. The submicron-sized grains will contribute to scattering some phonons with micron-range mean free paths. Furthermore, nanosized-grains—with a typical size smaller than 100 nm—appear at the grain boundaries and also inside grains. These nano-grains have a different chemical composition as concluded by the EADX analysis within the STEM. It shows that these nano-grains are Bi-poor grains, Sb-rich precipitates as well as Te nanodots.[34] Fig. 4c shows an example of nano-precipitates of 30 nm at the grain boundaries. At higher magnification (Fig. 4d), the crystalline orientation adjacent to the nano-precipitates varies significantly, promoting phonon grain boundary scattering.

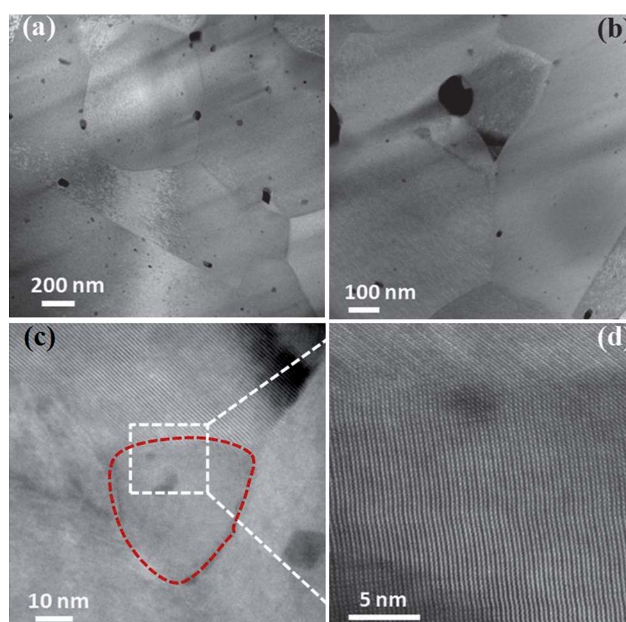

Fig. 4 TEM images obtained using a Fischione high angle annular dark detector (HAADF) at different magnification: (a) and (b) microstructure of multigrains, (c) image of nanoprecipitate or nanodot (outlined in red) detected at the intersection of multigrains, (d) HRTEM image showing the high angle grain boundary corresponding to the interface of nano-sized precipitates.

3.2. Structural and electrical characterisation with AFM and C-AFM

Fig. 5a shows the topography image in height mode using the diamond coated tip on sample S2. The surface is found to be very smooth with an RMS of 8 nm over a large area of 80 × 80 μm which complies with the results expected for CMP polishing (Fig. 5b). At high magnification, the microstructure of the sample is clearly identified using both height (Fig. 5c) and friction modes (Fig. 5d). It is important to note that the roughness of the surface within single grains is less than 1 nm. The grain size is in the range of 1–3 μm and is in good agreement with SEM imaging (Fig. 1c). The assignment of the grains is the result of chemical etching during the CMP step that causes height variation of the grains. The variation of the etching rate can be the result of several factors such as chemical composition, crystalline orientation and mechanical properties of the grains.

In addition to these observations, some grains in the submicron-size are identified in the AFM images. All of these grains have a polygonal shape. Furthermore, some nano-sized holes are found on the surface and mainly at the grain boundaries (Fig. 5c). By comparing the AFM images with the STEM ones

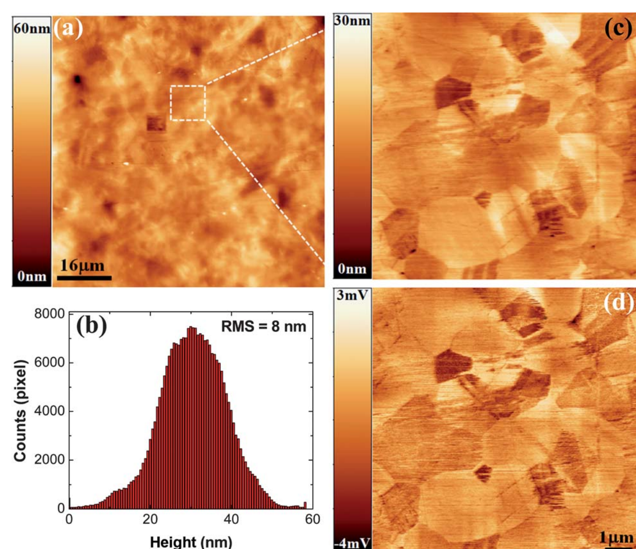

Fig. 5 AFM images obtained on a CMP polished sample by using diamond coated tips: (a) a low magnification AFM image 80 × 80 μm and (b) its corresponding height histogram. The surface after CMP is very smooth with an RMS of 8 nm for an 80 μm scan. (c) A high magnification topography image and its corresponding (d) lateral force image of the inset in Fig. 2a. The microstructure of the sample is obtained by AFM with high resolution, and we notice the presence of sub-micron grains.

(Fig. 4a), one can conclude that these holes correspond to nano-sized precipitates. This observation is useful to explain the C-AFM data (see below).

Fig. 6a shows the typical current map obtained by means of C-AFM with a diamond coated tip on sample S2 (after CMP polishing). The applied voltage is 5 mV and the tip–surface load is estimated to be 100 nN. Better assignment of the grains is recorded on C-AFM maps, in comparison with topography AFM images. Besides the micro-sized grains, some grains in the sub-micron range size, from 800 down to 100 nm (these grains are marked with dark dots in Fig. 6a), are observed.

Fig. 6b shows that the electrical current (extracted from Fig. 6a) exhibits a Gaussian distribution centred at 0.33 μA. This leads to a mean resistance of 14 kΩ. Using eqn (3) (see Section 2.3), the mean electrical conductivity of sample S2 is estimated to be 150 S cm^{-1}. Moreover, the maximum electrical conductivity of the same sample S2 (within the recorded C-AFM images) is approximately 470 S cm^{-1}. These values are in the range of the reported data on $(Bi,Sb)_2Te_3$ based nanocomposites and nanostructures.[35–37] However, the overall electrical conductivity of the same sample, measured by a macroscopic four probe technique, is about 1000 S cm^{-1}.[25]

The reasons accounting for this variation in results of electrical conductivity between the macro-scale and nano-scale are several; the most prominent of which should be the fact that the intrinsic electrical conductivity of the diamond tip (in the range of 200 to 350 S cm^{-1}) limits the measured resistance of the nano-contact.

At this point, it is important to note that the C-AFM technique is usually used for qualitative analysis. Indeed, the surface roughness and the conductive tip are convoluted, causing the contact areas to constantly change. In the present case study, the roughness of the sample, within one grain, is very low in comparison with the conductive tip's radius, making possible the estimation of the electrical conductivity with C-AFM.

Besides these limitations, the electrical conductivity measured on the nano-sized grains (size > 100 nm) seems to be in the range of those measured on the micro-sized grains. This means that the presence of nano-grains, although responsible for the strong decrease in the thermal conductivity, does not affect the electrical conductivity. This is one of the reasons behind the enhancement of the ZT value of the nanocomposite sample in comparison to its bulk counterpart. Moreover, the variation of the electrical conductivity from one grain to another may be correlated to the differential etching rate resulting from a large difference in crystalline orientation. The strong variation in the texture and crystalline orientation of adjacent grains also promotes the phonon scattering significantly.

It is important to point out the absence of sub-100 nm grains or precipitates on the recorded C-AFM images on sample S2. This is due to the removal of precipitates and nano-grains during the CMP step, which is in good agreement with the presence of nano-holes at the grain boundaries (Fig. 5c).

To be able to investigate the nano-sized grains with C-AFM and to overcome the limitation of the intrinsic resistance of the tip, a sharp and wear resistive metallic tip is employed, a silicon tip coated with 15 nm of iridium as a conductive coating layer. Moreover the sample S1 is studied to eliminate the possibility of passivation during the CMP process and removal of the nano-precipitates. Fig. 7a shows a typical current map obtained by probing a 1 × 1 μm area under a bias of 1 mV and load of 20 nN. A statistical study on several similar images (from seven different areas) reveals that more than 50% of the grains have a size lower

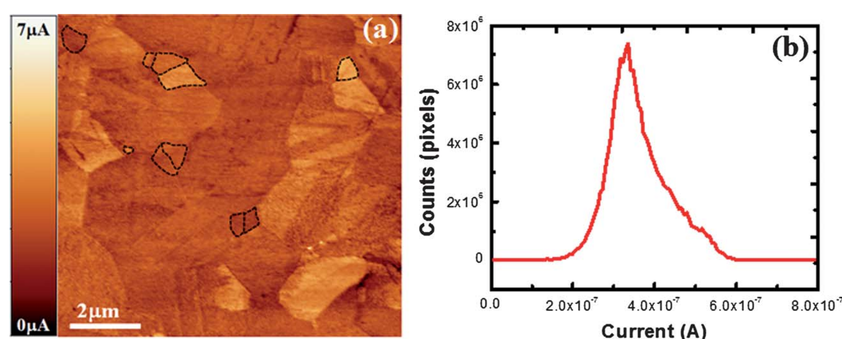

Fig. 6 (a and b) Current C-AFM map and its corresponding current histogram obtained on the CMP polishing sample by using a diamond coated tip. In the current map some sub-micron and nano-sized grains appear.

Downloaded by Massachusetts Institute of Technology on 15 June 2012
Published on 06 December 2011 on http://pubs.rsc.org | doi:10.1039/C1NR11366F

 This journal is © The Royal Society of Chemistry 2012

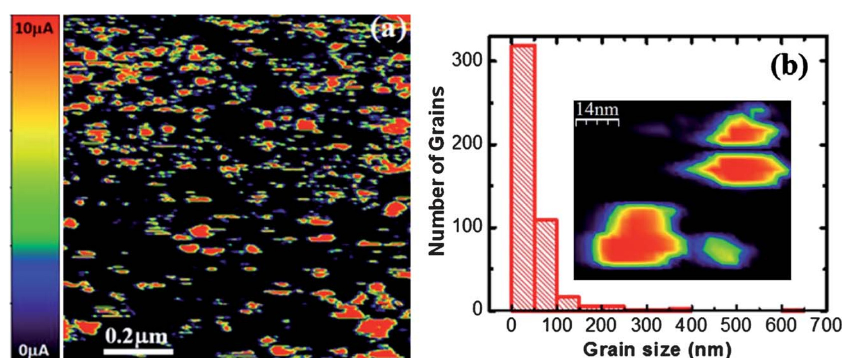

Fig. 7 (a) Current C-AFM map obtained on mechanically polished sample by using an iridium tip. These nano-sized grains and nano-precipitates are found to be more electrically conductive than the micro-sized grains. The histogram of grain size (b), extracted from different current-maps, shows that the typical size of nano-precipitates is less than 150 nm. In the inset of the histogram (d) an example of a high resolution C-AFM image is shown displaying four nano-precipitates with sizes less than 30 nm.

Published on 06 December 2011 on http://pubs.rsc.org | doi:10.1039/C1NR11366F
Downloaded by Massachusetts Institute of Technology on 15 June 2012

than 100 nm (Fig. 7b). Within these nano-grains, the average size lies between 20 nm and 40 nm. In the inset of Fig. 7b, an example of polygonal nano-grains with sub-20 nm sizes is illustrated.

Comparing C-AFM and STEM images, we conclude that these nano-size grains correspond to the Bi and Sb rich nano-precipitates and Te nano-dots. Furthermore, the most important result is that the nano-sized grains are observed to be more electrically conductive than the micro-sized grains. In fact, the electrical conductivity estimated (using the method described in Section 2.3) on these nano-structures is even higher than 1600 S cm^{-1}.

The existence of these nano-precipitates and nano-grains explains very well the low thermal conductivity of the $(Bi,Sb)_2Te_3$ nanocomposite which is estimated at 0.97 W mK^{-1} at room temperature using time domain and frequency domain thermoreflectance (TDTR and FDTR) measurements (results not shown). These nanostructures contribute to the scattering of phonons with a mean free path greater than the size of the grains and thus decrease the lattice thermal conductivity. Moreover, the C-AFM results show that nano-sized precipitates and nano-dots have higher electrical conductivity than the bulk value, thus enhancing the ZT value. The reasonable explanation of enhancement of the electrical conductivity (σ) on the $(Bi,Sb)_2Te_3$ nanocomposite, which is a p-type semiconductor, lies in the increased concentration of hole and ion vacancies. The Hall effect measurements at room temperature confirm that the hole carrier concentration of the nanograined material is 39% higher than that of the ingot. It is well known that the Bi vacancy donates three holes. Thus, the increase of the Bi vacancies inside the Bi-poor grains promotes the creations of the hole carriers. The increase of the concentration of holes inside the grain could be the reason for the enhancement of the electrical conductivity of the nano-precipitates and nanodots.

IV. Conclusions

In summary, we have performed a detailed analysis of the microstructure and the electrical conductivity of p-type nanograined bulk bismuth antimony telluride, $(Bi,Sb)_2Te_3$, with a peak ZT of 1.4 at 100 °C. Both AFM topography and C-AFM current reveal the microstructure of the surface with submicron resolution. These SPM techniques require minimal sample preparation in comparison to TEM. The image analysis suggests that the $(Bi,Sb)_2Te_3$ nanocomposite consists of grains with sizes distributed from 10 nm to 3 μm with high variation of crystalline orientation. This unique structure contributes to promote the grain boundary scattering, thereby decreasing the thermal conductivity to below 1 W mK^{-1} at room temperature. Moreover, the nano-sized precipitates and nanodots, with a size smaller than 100 nm, are found to be more electrically conductive than the bulk value. We suggest that the increase of electrical conductivity is related to the increase of Bi vacancies inside the grains, thereby increasing the concentration of the holes. This unique microstructure leads to an increase of the electrical conductivity while simultaneously decreasing the thermal conductivity, resulting in a high ZT. Moreover, the CMP operation, while revealing the microstructure and reducing the roughness, may decrease the interfacial electrical conductivity by passivating the surface. Based on this work, more experiments and investigation may be carried out for a complete understanding of the interfacial effect on the electrical and thermal contact resistances of nanocomposite Bi_2Te_3 based alloys.

References

1 D. Kraemer, B. Poudel, H.-P. Feng, J. C. Caylor, B. Yu, X. Yan, Y. Ma, X. Wang, D. Wang, A. Muto, K. McEnaney, M. Chiesa, Z. Ren and G. Chen, *Nat. Mater.*, 2011, **10**, 532–538.
2 D. M. Rowe, *CRC Handbook of Thermoelectrics: from Micro to Nano*, CRC Press, Boca Raton, FL, 2006.
3 A. M. Pettes, R. Melamud, S. Higuchi and K. E. Goodson, in *International Conference on Thermoelectrics*, 2007, p. 283.
4 L. W. da Silvia and M. Kaviany, *Int. J. Heat Mass Transfer*, 2004, **47**, 2417.
5 H. P. Freng, B. Yu, S. Chen, K. Collins, C. He, Z. F. Ren and G. Chen, *Electrochim. Acta*, 2011, 3079–3084.
6 M. G. Kanatzidis, *Chem. Mater.*, 2010, **22**, 869.
7 J. Martin, G. S. Nolas, W. Zhang and L. Chen, *Appl. Phys. Lett.*, 2007, **99**, 222112.
8 J. Martin, L. Wang, L. Chen and G. S. Nolas, *Phys. Rev. B: Condens. Matter Mater. Phys.*, 2009, **79**, 115311.
9 A. Popescu, L. M. Woods, J. Martin and G. S. Nolas, *Phys. Rev. B: Condens. Matter Mater. Phys.*, 2009, **79**, 205302.
10 R. Venkatasubramanian, E. Siivola, T. Colpitts and B. O'Quinn, *Nature*, 2001, **413**, 597.
11 T. Kong, S. B. Cronin and M. S. Dresselhaus, *Appl. Phys. Lett.*, 2000, **77**, 1490.
12 Y. Zhao, J. S. Dyck, B. M. Hernandez and C. Burda, *J. Am. Chem. Soc.*, 2010, **132**, 4982.

13 J. M. O. Zide, D. Vashaee, Z. X. Bian, G. Zeng, J. E. Bowers, A. Shakouri and A. C. Gossard, *Phys. Rev. B: Condens. Matter Mater. Phys.*, 2006, **74**, 205335.
14 R. G. Yang and G. Chen, *Phys. Rev. B: Condens. Matter Mater. Phys.*, 2004, **69**, 195316.
15 M. S. Dresselhaus, G. Chen, M. Y. Tang, R. G. Yang, H. Lee, D. Z. Wang, Z. F. Ren, J. P. Fleurial and P. Gogna, *Adv. Mater.*, 2007, **19**, 1043.
16 B. Poudel, Q. Hao, Y. Ma, Y. C. Lan, A. Minnich, B. Yu, X. Yan, D. Z. Wang, A. Muto, D. Vashaee, X. Y. Chen, J. M. Liu, M. S. Dresselhaus, G. Chen and Z. F. Ren, *Science*, 2008, **320**, 634.
17 T. Souier, F. Martin, C. Bataillon and J. Cousty, *Appl. Surf. Sci.*, 2010, **256**, 2434–2439.
18 F. Houze, R. Meyer, O. Schneegans and L. Boyer, *Appl. Phys. Lett.*, 1996, **69**, 1975–1977.
19 D.-Z. Guo, S.-M. Hou, G.-M. Zhang and Z.-Q. Xue, *Appl. Surf. Sci.*, 2006, **252**, 5149–5157.
20 W. Frammelsberger, G. Benstetter, J. Kiely and R. Stamp, *Appl. Surf. Sci.*, 2006, **252**, 2375–2388.
21 S. Berny, L. Tortech, M. Veber and D. Fichou, *ACS Appl. Mater. Interfaces*, 2010, **2**, 3059–3068.
22 A. Alkhatib, T. Souier and M. Chiesa, *Thin Solid Films*, 2011, **520**, 656–661.
23 J. M. Beebe, B. Kim, C. D. Frisbie and J. G. Kushmerick, *ACS Nano*, 2008, **5**, 827–832.
24 S. Santos and N. H. Thomson, *Appl. Phys. Lett.*, 2011, **98**, 013101–013103.
25 S. Santos, A. Verdaguer, T. Souier, H. N. Thomson and M. Chiesa, *Nanotechnology*, 2011, **22**, 465705–465713.
26 S. Santos, V. Barcons, J. Font and N. H. Thomson, *Nanotechnology*, 2010, **21**, 225710–225720.
27 D.-Z. Guo, S.-M. Hou, G.-M. Zhang and Z.-Q. Xue, *Appl. Surf. Sci.*, 2006, **252**, 5149–5157.
28 R. Holm, *Electric Contacts Handbook*, Springer, Berlin, 1958, p. 17.
29 Y. V. Sharvin, *J. Exp. Theor. Phys.*, 1965, **21**, 655.
30 G. Wexler, *Proc. Phys. Soc.*, 1966, **89**, 927.
31 B. Nikolic and Ph. B. Allen, *Phys. Rev. B: Condens. Matter*, 1999, **60**, 3963.
32 A. Mavrokefalos, A. L. Moore, M. T. Pettes, L. Shi, W. Wang and L. Xiaoguang, *J. Appl. Phys.*, 2009, **105**, 104318.
33 B. V. Derjaguin, V. M. Muller and Y. P. Toporov, *J. Colloid Interface Sci.*, 1975, **53**, 314.
34 Y. Lan, B. Poudel, Y. Ma, D. Wang, M. S. Dresselhaus, G. Chen and Z. Ren, *Nano Lett.*, 2009, **9**, 1419–1422.
35 Y. Zhao, J. S. Dyck, B. M. Hernandez and C. Burda, *J. Phys. Chem. C*, 2010, **114**, 11607–11613.
36 Y. Ma, Q. Hao, B. Poudel, Y. Lan, B. Yu, D. Wang, G. Chen and Z. Ren, *Nano Lett.*, 2008, **8**(no. 8), 2580–2584.
37 Y. Q. Cao, X. B. Zhao, T. J. Zhu, X. B. Zhang and J. P. Tu, *Appl. Phys. Lett.*, 2008, **92**, 143106.

Downloaded by Massachusetts Institute of Technology on 15 June 2012
Published on 06 December 2011 on http://pubs.rsc.org | doi:10.1039/C1NR11366F

This journal is © The Royal Society of Chemistry 2012